J. Fluid Mech. (2024), *vol*. 986, A15, doi:10.1017/jfm.2024.346

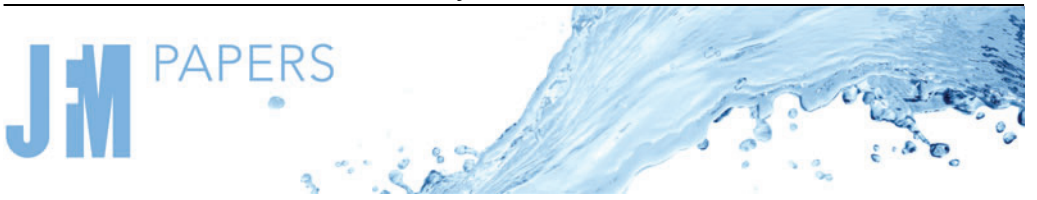

Vortex-induced rotation of a square cylinder under the influence of Reynolds number and density ratio

Rui-Yong Mou[1,2], **Wei-Xi Huang**[3], **Xing-Rong Huang**[2] **and Le Fang**[2,†]

[1]Research Institute of Aero-Engine, Beihang University, Beijing 100191, PR China

[2]LCS, Ecole Centrale de Pékin, Beihang University, Beijing 100191, PR China

[3]School of Aerospace Engineering, Tsinghua University, Beijing, 100084, PR China

(Received 4 October 2023; revised 25 February 2024; accepted 1 April 2024)

Numerical simulations are carried out on the vortex-induced rotations of a freely rotatable rigid square cylinder in a two-dimensional uniform cross-flow. A range of Reynolds numbers between 40 and 150 and density ratios between 0.1 and 10 are considered. Results show eight different characteristic regimes, expanding the classification of Ryu & Iaccarino (*J. Fluid Mech.*, vol. 813, 2017, pp. 482–507). New regimes include the transition and wavy rotation regimes; in the π-limited oscillation regime we observe multipeak subregimes. Moment-generating mechanisms of these regimes and subregimes are further elucidated. A phenomenon related to the influence of density ratio is the tooth-like shape of the $\pi/2$-limit oscillation regime observed in the regime map, which is explained as a result of the imbalance relation between the main frequencies of rotation response and the vortex shedding frequency. In addition, existence of multiple regimes and multistable states are discussed, indicating multiple stable attractive structures in phase space.

Key words: flow-structure interactions, vortex shedding

1. Introduction

Fluid–structure interactions lead to many important phenomena in engineering applications, including the vortex-induced vibrations (VIVs) and vortex-induced rotations (VIRs). Both VIVs and VIRs are simplified but fundamental models for understanding the mechanisms of fluid–structure interactions. In this section we will briefly revisit the literature to explain the related concepts, and to clarify the motivation of the present study.

† Email address for correspondence: le.fang@buaa.edu.cn

There have been extensive experimental and numerical investigations on VIVs in past years (Sarpkaya 2004; Williamson & Govardhan 2004). In these studies, circular cylinder is the simplest model but can already lead to typical VIV phenomena. Griffin (1985) and Williamson & Roshko (1988) investigated systematically the fluctuating lift and drag forces on a two-dimensional cylinder in a uniform cross-flow, coupled with the alternate vortex shedding with three typical patterns, i.e. the 2S mode, 2P mode and P+S mode, respectively. These results were validated by using numerical simulations (Minewitsch, Franke & Rodi 1994; Taylor & Vezza 1999). As one of the most interesting phenomena of VIVs, the frequency lock-in has been systematically studied. As an example, considering the transverse oscillation of a circular cylinder, discussions on the parameter influences can be found in Bearman (2011). Towards complicated reality, there have also been many studies on the VIVs of square cylinders (Cheng, Zhou & Zhang 2003; Amandolèse & Hémon 2010; Bao, Wu & Zhou 2012; Jiang *et al.* 2016; Zhang *et al.* 2018; Han & de Langre 2022; Qiu *et al.* 2022) and multiple objects (Mittal, Kumar & Raghuvanshi 1997; Assi, Bearman & Meneghini 2010). By comparing with a single circular cylinder, these results reveal more complicated VIVs, where the responses of objects are affected by additional setting parameters.

On the other hand, the investigations on VIRs are not so broad by comparison with VIVs. There exist some investigations on the VIRs of typical shapes of freely rotating cylinders, such as circular cylinders (Juarez *et al.* 2000), triangular cylinders (Wang *et al.* 2011, 2019) and rectangular cylinders (Robertson *et al.* 2003). However, the most common model for studying VIRs is to use square cylinders. Early experimental and numerical studies by Zaki, Sen & Gad-El-Hak (1994) recognized four typical modes of square cylinder response, i.e. static stability, oscillation, reverse rotation and autorotation, respectively. A systematic study was performed by Ryu & Iaccarino (2017) and enriched the response modes into six characteristic regimes through a parameter investigation, i.e. stable, small-amplitude oscillation, $\pi/2$-limit oscillation, random rotation, π-limit oscillation and autorotation regimes, respectively. Comparing with Zaki *et al.* (1994), this classification showed more details and complexities at moderate Reynolds numbers, by discussing the phase synchronization/differences between the moment generation and angle of rotation in different regimes. There also exist other studies considering more complicated cases, such as the combination of square cylinders (Shao *et al.* 2019) and rotation in a microchannel (Pan, Chen & Wu 2019). Similar to the VIVs, these complicated settings lead to different response of the square cylinder, but the responses were not beyond the classification of Ryu & Iaccarino (2017). In the present paper we will show more complicated response of a single cylinder by expanding the parameter space. In fact, Ryu & Iaccarino (2017) remarked that the rotational inertia of a square cylinder, which can also be dimensionlessly parameterized to the density ratio between cylinder and fluid, might also affect the dynamics responses of a square cylinder, but almost all existing studies used a constant rotational inertia. Expanding the parameter space by considering the change of rotational inertia will then be performed in the present paper, aiming at revealing new response modes and underlying mechanisms in VIRs.

Some phenomena of VIRs are analogous to VIVs, for example, the small-amplitude oscillation regime of square cylinders can also be considered as an angular vibration and analytically predicted by introducing a free-streamline boundary-layer model (Luo *et al.* 2023), where the elastic force is not generated by a solid property, but is the result of a flow field. In this sense, the autorotation regime shows its particularity by comparing with the phenomena in VIVs and has attracted many investigations, for example Lugt (1980, 1983), Ryu (2018) and Xia *et al.* (2018). In the present paper, we will also contribute to

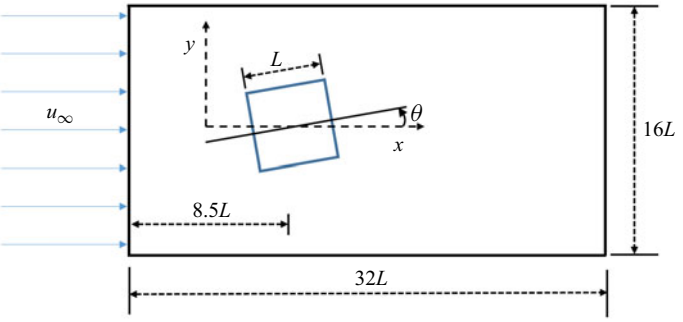

Figure 1. Schematic diagram of rigid square cylinder moving in a uniform flow with velocity u_∞.

this understanding. Specifically, we will show a 'wavy rotation' regime, which is similar to the autorotation regime but contains periodically short-time back swing.

This paper is organized as follows: the problem formation and computational method are described in § 2; the results and discussion are presented in § 3; finally, in § 4 we give the conclusions.

2. Problem description and numerical method

In the present paper, we consider a two-dimensional case that a uniform incompressible flow passes and interacts with a freely rotatable rigid square cylinder, as sketched in figure 1. The streamwise and normal directions are denoted as x and y, respectively. The square cylinder, with side length L, can freely rotate around its centre O, which is located $8.5L$ from the inlet in the streamwise direction, and in the centre in the normal direction. The computational domain size is $32L \times 16L$, with all boundaries having the free stream velocity condition, i.e. $\boldsymbol{u} = (u_\infty, 0)$ with $\boldsymbol{u}$ being the flow velocity. The flow field is governed by the incompressible Navier–Stokes equations,

$$\nabla \cdot \boldsymbol{u} = 0, \tag{2.1}$$

$$\rho_0 \left(\frac{\partial \boldsymbol{u}}{\partial t} + \boldsymbol{u} \cdot \nabla \boldsymbol{u} \right) = -\nabla p + \mu \Delta \boldsymbol{u} + \boldsymbol{f}, \tag{2.2}$$

with flow parameters ρ_0 the fluid density and μ the dynamics viscosity. Here t is the time, p is the pressure and $\boldsymbol{f}$ is the momentum forcing applied to enforce the no-slip boundary condition along the immersed boundary.

According to the theorem of angular momentum, the governing equation for a freely rotatable rigid body is

$$I \frac{\mathrm{d}^2\theta}{\mathrm{d}t^2} = T, \tag{2.3}$$

where I is the moment of inertia about the centre of the cylinder, θ is the rotation angle and $T = |\boldsymbol{T}|$ is the torque exerted on the mass by the fluid. For the case of a square cylinder we can write

$$I = \rho_s L^4/6, \tag{2.4}$$

$$\boldsymbol{T} = \int_\Gamma \boldsymbol{F} \times \boldsymbol{X}_r \, \mathrm{d}s, \tag{2.5}$$

where ρ_s is the density of the cylinder, Γ is the boundary of the cylinder, $\boldsymbol{F}$ is the Lagrangian force exerted on the cylinder surface and $\boldsymbol{X}_r$ is the displacement vector with the centre of the cylinder. Substituting (2.4) into (2.3) leads to

$$T = \frac{1}{6}\rho_s L^4 \frac{\mathrm{d}^2\theta}{\mathrm{d}t^2}. \tag{2.6}$$

The non-dimensionalization on the above equations is performed by introducing the following characteristic scales: u_∞ for velocity; L for length; ρ_0 for fluid density; L/u_∞ for t; $\rho_0 u_\infty^2$ for p; $\rho_0 u_\infty^2/L$ for $\boldsymbol{f}$; $\rho_0 u_\infty^2$ for $\boldsymbol{F}$; $\rho_0 L^4$ for I; $\rho_0 u_\infty^2 L^2$ for $\boldsymbol{T}$. The non-dimensional governing equations are therefore

$$\frac{\partial \boldsymbol{u}^*}{\partial t^*} + \boldsymbol{u}^* \cdot \nabla^* \boldsymbol{u}^* = -\nabla^* p^* + \frac{1}{Re}\Delta^* \boldsymbol{u}^* + \boldsymbol{f}^*, \tag{2.7}$$

$$\frac{1}{6}\rho \frac{\mathrm{d}^2\theta}{\mathrm{d}t^{*2}} = T^*, \tag{2.8}$$

where $Re = \rho_0 u_\infty L/\mu$ is the Reynolds number, and $\rho = \rho_s/\rho_0$ is the non-dimensional solid density. The initial condition of the cylinder is set as $\theta|_{t=0} = \theta_0$ and $\mathrm{d}\theta/\mathrm{d}t|_{t=0} = 0$.

The interaction between the fluid and the immersed boundary is described by introducing the Lagrangian force, calculated as

$$\boldsymbol{F}^* = \alpha \int_0^{t^*} (\boldsymbol{U}_{ib}^* - \boldsymbol{U}_s^*)\,\mathrm{d}t' - \beta(\boldsymbol{U}_{ib}^* - \boldsymbol{U}_s^*), \tag{2.9}$$

where α and β are negative constants, $\boldsymbol{U}_s^*$ is the velocity of the cylinder boundary and $\boldsymbol{U}_{ib}^*$ is the fluid velocity obtained by interpolation at the immersed boundary, which is expressed as

$$\boldsymbol{U}_{ib}^*(s,t) = \int_\Omega \boldsymbol{u}^*(\boldsymbol{x},t)\delta(\boldsymbol{X}(s,t) - \boldsymbol{x})\,\mathrm{d}\boldsymbol{x} \tag{2.10}$$

with $\delta()$ the Dirac delta function (in calculations we use a smoothed delta function instead). The relation between Lagrangian force and Eulerian force is

$$\boldsymbol{f}^*(\boldsymbol{x},t) = \int_\Gamma \boldsymbol{F}^*(s,t)\delta(\boldsymbol{x} - \boldsymbol{X}(s,t))\,\mathrm{d}s. \tag{2.11}$$

The details on the immersed boundary method and numerical discretizations can be found in Huang, Shin & Sung (2007).

In order to verify the correctness of the calculation, we calculate the case where flow passes a fixed square cylinder. The Reynolds number is $Re = 100$. Mesh and calculation domain independence is verified in table 1. It is shown that when the calculation domain is larger than $16L \times 32L$, and the grid number is more than 512×1024, the aerodynamic performances, including the mean drag coefficient C_D, root-mean-square (r.m.s.) lift coefficient $C_{L,rms}$ and Strouhal number St, can converge.

To assess the accuracy of the code, we select the case with 512×1024 grids, in a $16L \times 32L$ calculation domain, and simulate a fixed, rigid square cylinder in a two-dimensional uniform cross-flow. Compared with the results in the literature, as shown in table 2, a good agreement can be observed to support the present calculations.

Further validations by comparing with Ryu & Iaccarino (2017) are performed at different Reynolds numbers, respectively, as shown in figure 2. In the insets we plot the

Calculation domain	Grid number	C_D	$C_{L,rms}$	St
$8L \times 8L$	256×256	2.3643	0.1705	0.1883
$8L \times 16L$	256×512	1.8267	0.1906	0.1650
$16L \times 32L$	512×1024	1.5874	0.1938	0.1477
$32L \times 64L$	1024×2048	1.5084	0.1805	0.1409
$16L \times 32L$	256×512	1.6585	0.1853	0.1433
$16L \times 32L$	512×1024	1.5874	0.1938	0.1477
$16L \times 32L$	1024×2048	1.5733	0.2006	0.1483

Table 1. Comparison of mean drag coefficient C_D, r.m.s. lift coefficient $C_{L,rms}$ and Strouhal number St under different computational domains and grid numbers. Reynolds number $Re = 100$.

$Re = 100$	C_D	$C_{L,rms}$	St
Arnal, Goering & Humphrey (1991)	1.39	—	0.14
Sohankar, Norbergb & Davidson (1997)	1.47	0.156	0.146
Cheng, Whyte & Lou (2007)	1.44	0.152	0.144
Yoon, Yang & Choi (2010)	1.4385	0.1774	—
Sen, Mittal & Biswas (2011)	1.5287	0.1928	0.1452
Park *et al.* (2015)	1.378	0.161	0.141
Ryu & Iaccarino (2017)	1.5642	0.1932	0.1506
The present calculation	1.5874	0.1938	0.1477

Table 2. Comparison of mean drag coefficient C_D, r.m.s. lift coefficient $C_{L,rms}$ and Strouhal number St with reference results, for the case that flow passes a fixed square cylinder. Reynolds number $Re = 100$. The present calculation is performed with 512×1024 grids, in a $16L \times 32L$ calculation domain.

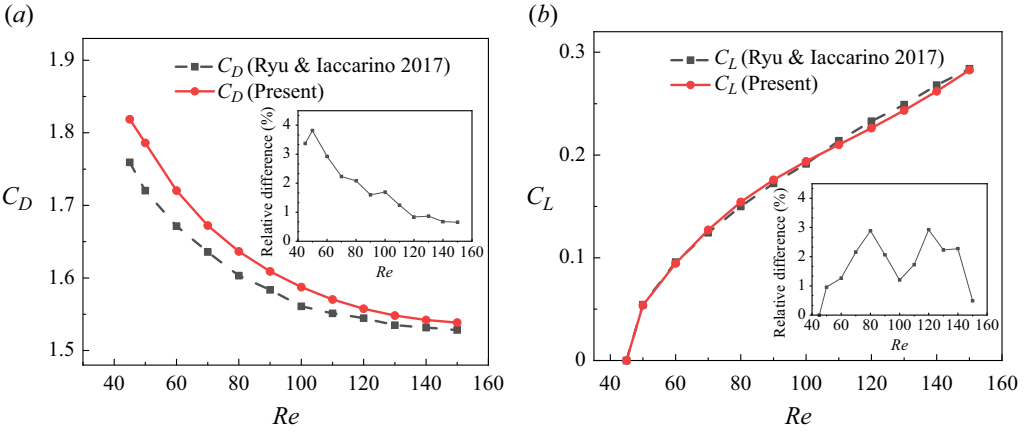

Figure 2. Comparison of (*a*) drag coefficient (*b*) lift coefficient with Ryu & Iaccarino (2017) at Reynolds number from 45 to 150, respectively. The insets show the relative difference between the present study and the reference work.

relative differences between them, which are always less than 4 %. This value is small by comparison with the literature (see table 2), indicating the correctness of the present results.

In the following parts, we perform calculations on the freely rotatable square cylinder under various parameters of $0.1 \leqslant \rho \leqslant 10$ and $40 \leqslant Re \leqslant 150$.

3. Results

In order to better describe and analyse the phenomena, here we first define two terms. Following Park *et al.* (2015), Ryu & Iaccarino (2017), Pan *et al.* (2019) and Shao *et al.* (2019), we use 'regime' to refer to the dynamic responses of the square cylinder; by contrast, the term 'region' is used to describe an area in the (ρ, Re) phase plane, for the ease of following discussions. As will be shown in the following parts, 'region' and 'regime' are not a bijection. We will discuss the regimes in § 3.1 and show the regime map by defining the regions in § 3.2.

3.1. *Regimes of dynamic responses of a square cylinder*

In this subsection we will summarize and classify the regimes we observed in calculations. We follow Ryu & Iaccarino (2017) to define six regimes, i.e. stable, small-amplitude oscillation, $\pi/2$-limit oscillation, random rotation, π-limit oscillation and autorotation regimes. Note that these definitions are not exactly the same as Ryu & Iaccarino (2017), for example, we observe different dynamic responses in the π-limit oscillation regime. Besides, we will show two new regimes, i.e. wavy rotation and transition regimes, which, to our knowledge, have not been reported in the literature.

These typical regimes are presented in figure 3, by selecting some typical combinations (ρ, Re). Their descriptions are listed as follows.

(*a*) The stable regime indicates that the initial perturbation is damped, and the square cylinder reaches a stable equilibrium point.

(*b*) The small-amplitude oscillation regime indicates that the square cylinder oscillates monoharmonically with small amplitudes less than 10^{-2}. This threshold value is consistent with Ryu & Iaccarino (2017).

(*c*) The $\pi/2$-limit oscillation regime indicates that the amplitude of the rotation angle is close to $\pm\pi/4$. In addition, multiharmonic oscillations can be observed.

(*d*) The transition regime can be considered as a mixture of the $\pi/2$-limit oscillation and random rotation regimes. Specifically, the regime randomly switches between different quasi-$\pi/2$-limit oscillation regimes with different quasiequilibrium angles.

(*e*) The random rotation regime indicates intermittent oscillations and rotations in a temporally random fashion. Comparing with the transition regime, no quasi-$\pi/2$-limit oscillation can be observed.

(*f*) The π-limit oscillation regime indicates another temporal oscillation of the cylinder with a rotation limit π. The cylinder may oscillate or rotate in a random fashion at the beginning, and then oscillates periodically. Note that Ryu & Iaccarino (2017) reported that the π-limit oscillation regime always contains a single bell-like curve in each period, but we also find other subregimes with multiple peaks and valleys in a period (see the dashed line in figure 3*f* as an example). The details of these phenomena will be analysed in § 3.4.3.

(*g*) The wavy rotation regime indicates that in a period, the cylinder rotates for a large angle in a certain direction and then reverses for a small angle. According to symmetry, the rotation direction of the cylinder can be clockwise or anticlockwise. In addition, we also find another subregimes of this regime which reverses two times in one period (see discussions later in § 3.4.2).

(*h*) The autorotation regime indicates that the cylinder undergoes random rotations at the beginning and then autorotates in one direction without reversal. According to symmetry, the rotation direction of the cylinder can be clockwise or anticlockwise.

3.2. *Overview of the region map of regimes*

Based on our calculations, we summarize the regimes under different Reynolds numbers and density ratios in figure 4. Each symbol corresponds to a numerical test case, while the different symbol styles are used to represent different regimes. Based on these results, we further divide the (ρ, Re) phase plane into six regions (contours in figure 4). Their descriptions are listed as follows.

Region (1) corresponds to the stable regime at $Re = 40$. Changing the value of ρ does not affect the regime.

Region (2) corresponds to the small-amplitude oscillation regime. Again, changing the value of ρ does not affect the regime.

Region (3) corresponds to the $\pi/2$-limit oscillation regime. According to figure 4, it is interesting that an irregular tooth-like shape is observed at $\rho = 5$ and $Re = 130, 140$. This phenomenon will be explained later in § 3.3.

Region (4) corresponds to both the transition and random rotation regimes. We classify these two regimes in the same region since both of them correspond to unstable motions of the cylinder.

Region (5) is complicated since there exists four regimes chaotically, i.e. random rotation, π-limit oscillation, wavy rotation and autorotation regimes. In figure 4 we present seven test cases as 'multiple regimes', but indeed we have calculated many more cases in this region and found that the results are quite uncertain. For instance, in figure 5 we show the regimes of 40 test cases for $Re = 140$ and $\rho \leqslant 4$. It can be observed that regimes are chaotic. In addition, we can observe different dynamics for the π-limit oscillation and wavy rotation regimes in this region, in which one period can contain multiple peaks. These different dynamics have not been discussed in the literature, and they will be named as 'subregimes' in the present study. The complexity in this region is also reflected from the fact that different initial angles of the cylinder can lead to different regimes (see discussions in § 3.5).

Region (6) corresponds to the autorotation regime.

We remark that Ryu & Iaccarino (2017) have defined a classification for the $\rho = 2$ cases. Here our classifications are principally consistent with Ryu & Iaccarino (2017), while the differences are mainly due to the slight differences in the definition of regimes.

In the following subsections, we will first discuss the tooth-like shape of the $\pi/2$-limit oscillation regime, and then visit in detail the typical regions in figure 4.

3.3. *Tooth-like shape in the regime map*

As summarized in § 3.2, an interesting phenomenon in the region map of regimes is the irregular tooth-like shape of region (3), which is located at $\rho = 5$ and $Re = 130, 140$. In order to understand why these parameters lead to the $\pi/2$-limit oscillation regime instead of the transition or random rotation regimes, an analysis of the frequency spectrum on the dynamic responses of the square cylinder is carried out.

At Reynolds number $Re = 120$, we select two typical cases with $\rho = 5$ and 6. It can be found from figure 4 that both cases lead to $\pi/2$-limit oscillation, hence it is possible to transfer the time evolution of the lift coefficient (shown in figures 6*a* and 6*b*,

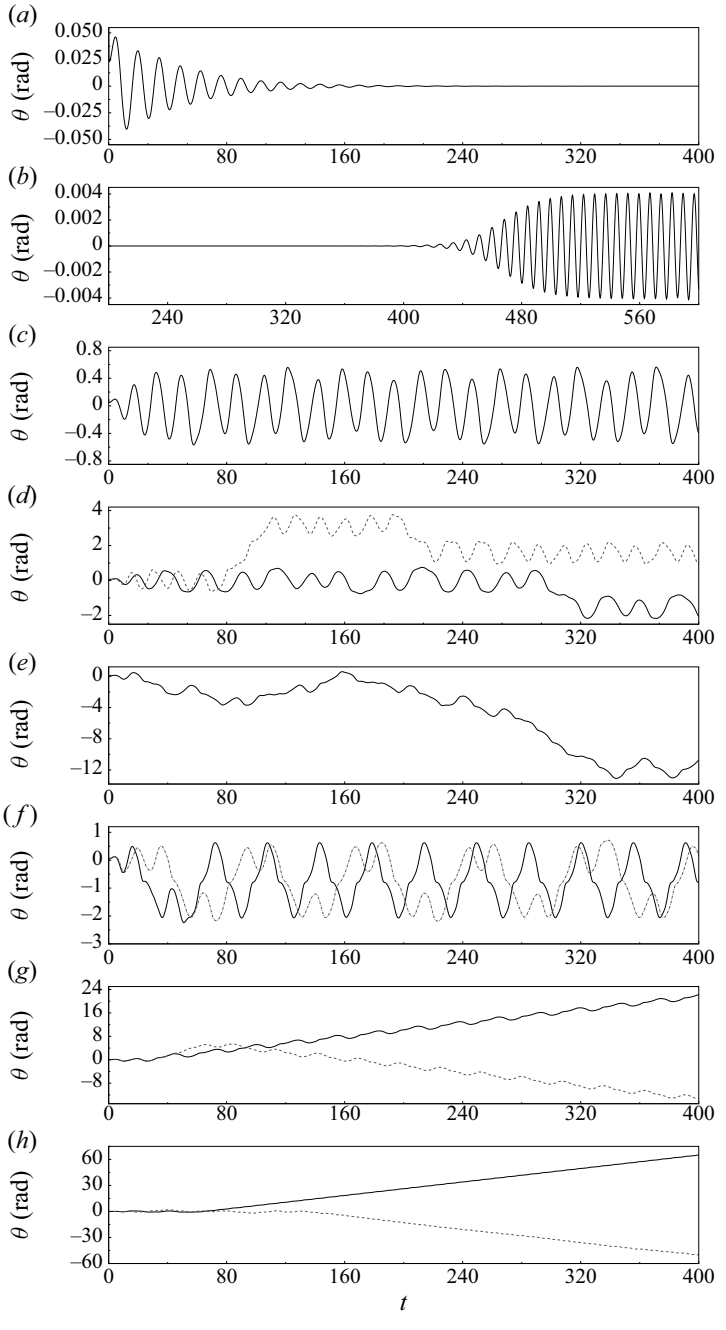

Figure 3. Time histories of rotation angle of typical regimes: (*a*) stable regime ($Re = 40$, $\rho = 2$); (*b*) small-amplitude oscillation regime ($Re = 70$, $\rho = 10$); (*c*) $\pi/2$-limit oscillation regime ($Re = 80$, $\rho = 2$); (*d*) transition regime (solid line, $Re = 90$, $\rho = 4$; dashed line, $Re = 100$, $\rho = 1$); (*e*) random rotation regime ($Re = 100$, $\rho = 2$); (*f*) π-limit oscillation regime (solid line (1-peak subregime), $Re = 130$, $\rho = 1$; dashed line (2-peak subregime), $Re = 140$, $\rho = 3.1$); (*g*) wavy rotation regime (solid line, $Re = 140$, $\rho = 2.5$; dashed line, $Re = 140$, $\rho = 2.6$); (*h*) autorotation regime (solid line, $Re = 150$, $\rho = 2$; dashed line, $Re = 150$, $\rho = 0.1$).

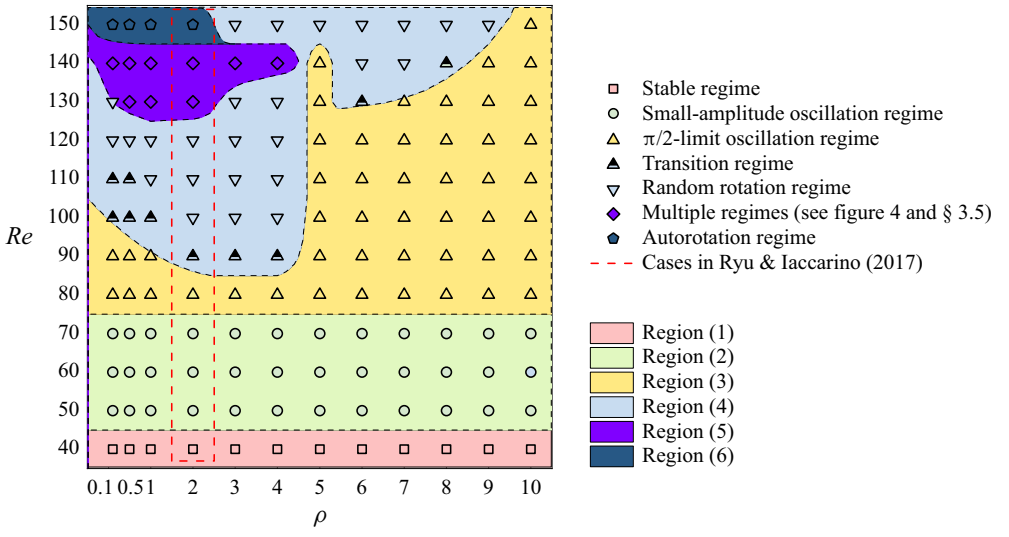

Figure 4. Overview of regimes on the (ρ, Re) phase plane. According to the regimes, the phase plane is further divided into six regions. The cases with $\rho = 2$ correspond to the set-up of Ryu & Iaccarino (2017).

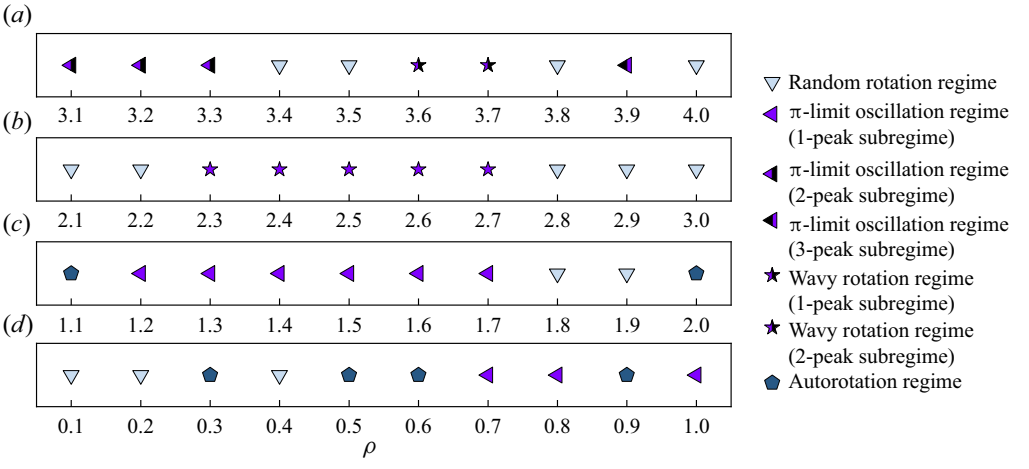

Figure 5. Regimes and subregimes for the cases of $Re = 140$, $\rho \leqslant 4$. Initial angle is selected as $\theta_0 = 0.1$.

respectively) to frequency space. As seen from figures 6(*c*) and 6(*d*), both cases have two main frequencies. This is qualitatively consistent with the observations of Ryu & Iaccarino (2017) for lower Reynolds number $Re = 90$, but here the two main frequencies have comparable amplitudes, rather than the quasimonofrequency responses in Ryu & Iaccarino (2017). In fact, in Ryu & Iaccarino (2017) the main frequency was shown to correspond to the vortex shedding frequency, while the small-amplitude small-frequency envelope was weak, and was not explained. By contrast, in our cases both frequencies have their amplitudes at the same order, leading to the transition to other complicated regimes.

Clearly, by naming the frequency of largest amplitude as 'basic frequency', and the other one as 'subfrequency', the comparison between figures 6(*c*) and 6(*d*) shows their different orders. We can perform the same operation on all cases with $\pi/2$-limit oscillation regime near the tooth-like shape in the regime map, as shown in table 3. It is interesting

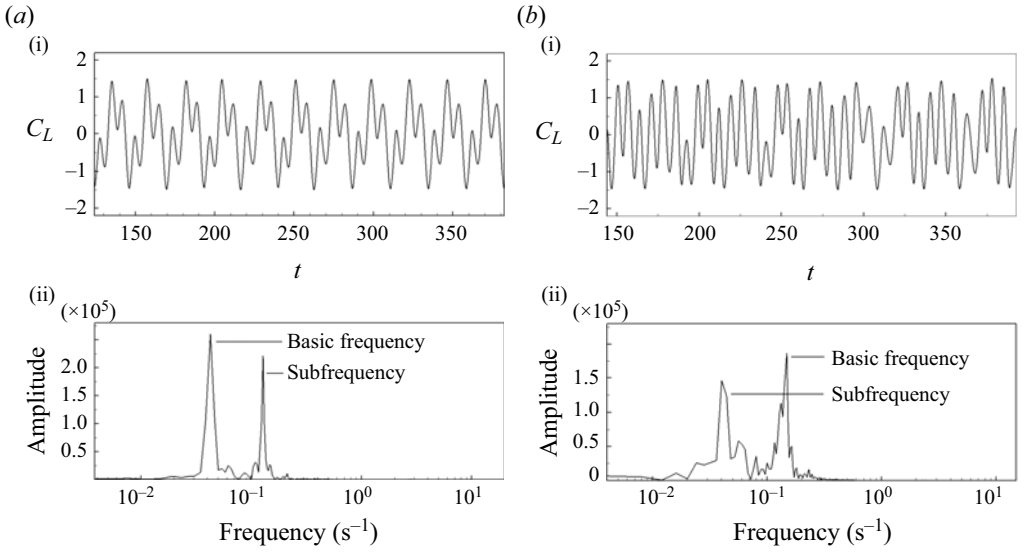

Figure 6. Comparison between (*a*) $Re = 120$, $\rho = 5$ and (*b*) $Re = 120$, $\rho = 6$, showing (i) the evolution of lift coefficient C_L and (ii) its frequency spectrum.

that for all the $\rho = 5$ cases the basic frequency is always smaller than the subfrequency, while for other cases it is the opposite. In table 3 we also use the reference frequencies of the lift coefficient evolution in the flow past a fixed circular cylinder (denoted as RF1) and square cylinders (denoted as RF2 and RF3) as references, which could approximately represent the frequencies of natural vortex shedding. It can be found that for the $\rho = 5$ cases the subfrequency is close to the reference frequencies, while for other cases the basic frequency is close to the reference frequencies. We can therefore explain that the transition from $\pi/2$-limit oscillation regime to other unstable regimes can be related to the interaction between the cylinder and the natural vortex shedding. For the $\rho \neq 5$ cases, the basic frequency is close to the reference frequencies, indicating that the influence of natural vortex shedding is dominant. Hence, increasing the Reynolds number will lead to instability of natural vortex shedding and then a change of the regime of the cylinder. By contrast, for the $\rho = 5$ cases the dominant factor for the cylinder response is a lower-frequency envelope, therefore the instability of natural vortex shedding will be more difficult to change the regime of the cylinder.

In brief, the comparison of the frequency with that of vortex shedding can explain the formation of the tooth-like shape of the $\pi/2$-limit oscillation regime.

3.4. *Moment-generating mechanisms of new regimes and subregimes*

As summarized in § 3.1, in the present study we have observed new regimes and subregimes for the cylinder responses. In this section we will follow the analysis method of Ryu & Iaccarino (2017), to show the underlying moment-generating mechanisms of these regimes and subregimes.

3.4.1. *Transition regime*

As shown in figure 3(*d*), the typical dynamics of the transition regime indicates that the regime randomly switches between different quasi-$\pi/2$-limit oscillation regimes with

$Re = 120$	$\rho = 5$	$\rho = 6$	$\rho = 7$	$\rho = 8$	RF1	RF2	RF3
Basic frequency	0.0425	0.145	0.1375	0.1425	0.17	0.154	0.154
Subfrequency	0.1275	0.0425	0.04	0.0375	—	—	—
$Re = 130$	$\rho = 5$	$\rho = 6$	$\rho = 7$	$\rho = 8$			
Basic frequency	0.0525	*	0.1425	0.145	0.173	0.156	0.156
Subfrequency	0.155	*	0.035	0.035	—	—	—
$Re = 140$	$\rho = 5$	$\rho = 6$	$\rho = 7$	$\rho = 8$			
Basic frequency	0.0534	*	*	0.145	0.177	0.158	0.157
Subfrequency	0.1602	*	*	0.0325	—	—	—

Table 3. Comparison of main frequencies of lift coefficient evolution in different cases. Here, RF1 refers to the reference frequency of lift coefficient evolution in the flow past a fixed circular cylinder (Williamson 1989); RF2 and RF3 refer to the reference frequency of lift coefficient evolution in the flow past a fixed square cylinder with angle 0 and $\pi/4$, respectively. The sign * corresponds to transition or random rotation regimes without any main frequency.

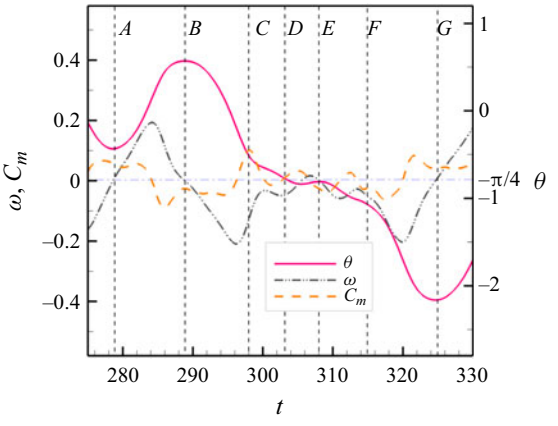

Figure 7. Time histories of the rotation angle θ, angular velocity ω and moment coefficient C_m, in the switch procedure of transition regime ($Re = 90$, $\rho = 4$).

different quasiequilibrium angles. Since the dynamics of the $\pi/2$-limit oscillation regime has already be analysed with substantial details in Ryu & Iaccarino (2017), here we will emphasize the switch procedure and the corresponding moment-generating mechanisms, as presented in figure 7. In the figure we show the time history of the rotation angle (θ), the non-dimensional angular velocity ω (defined as $\omega^* L/u_\infty$) and the moment coefficient C_m (defined as $2T^*/\rho_0 u_\infty^2 L^2$). Seven typical instants (A–G) are marked. Between A and C, the square cylinder is driven by the out-of-phase synchronized moments, as the same as the $\pi/2$-limit oscillation regime described by Ryu & Iaccarino (2017). However, between C and F the behaviour is different, where ω and C_m are close to zero and change slowly, corresponding to a quasiequilibrium point with instable properties. Finally, after F the system switches to another $\pi/2$-limit oscillation regime with a new quasiequilibrium angle.

Figure 8 shows the pressure and spanwise vorticity contours with streamlines at six instants (B to G) marked in figure 7. At B, two recirculation zones are observed on the leeward surfaces of the cylinder, the same as the $\pi/2$-limit oscillation regime of Ryu & Iaccarino (2017). At C, the cylinder has rotated by approximately $\pm\pi/4$ clockwise.

The stagnation pressure pocket is now near corner 'p', which produces an anticlockwise moment. As shown in figure 7, the moment reaches its maximum and the magnitude of angular velocity decreases rapidly as a consequence. The flow patterns in the downstream wake region in A to C fall into the 2S mode, and a regular von Kármán vortex street with uniform intensity of the shed vortices is observed, the same as the $\pi/2$-limit oscillation regime of Ryu & Iaccarino (2017).

At D we can clearly observe the vortex shedding. The position of the stagnation pressure pocket does not generate a significant rotational moment, so the moment at D is close to zero. However, compared with A, the angular velocity at D is stronger, leading to the vortex shedding by inertia.

From D to E, the rotation angle fluctuates around $-\pi/4$, while the moment and angular velocity fluctuate around zero. At E the recirculation zone is located near the lower part of the wake region. However, the net moment is in the clockwise direction and drives the cylinder towards clockwise rotation.

At F, the cylinder overcomes the asymptotic limit ($-\pi/4$) and keeps rotating. The stagnation pressure pocket is now located near corner 'q' and generates a clockwise moment that drives the cylinder towards clockwise rotation. The flow pattern is the asymmetric P+S mode from D to F (as displayed with red circles in figure 8*h*). By contrast, the flow patterns in the downstream wake region in G return to the 2S mode, as displayed with red circles in figure 8(*l*).

Furthermore, we compare the transition regime with the $\pi/2$-limit oscillation regime in figure 9. Note that in order to better account for differences in the moments of inertia between the two regimes, here we present the angular acceleration α (which equals to $C_m/2I$) instead of the moment. We choose the similar starts and observe the difference afterwards. As shown in figure 9, between instants A and C, the angle and angular acceleration of the two regimes are nearly synchronous. Between instants C and F, the $\pi/2$-limit oscillation repeats periodically while the transition regime switches to another quasi-$\pi/2$-limit oscillation regime with a different quasiequilibrium angle. The initial difference happens from B to C, in which the angular acceleration of the transition regime is lower than that of the $\pi/2$-limit oscillation regime. This leads to a slower and clockwise variation of the angular velocity for the transition regime, and finally yields the inverse rotations between the two regimes at C. In the transition regime, the cylinder then continues to rotate and cross the $-\pi/4$ asymptotic limit. We can also explain the transition if we compare the quasi-$\pi/2$-limit oscillation of the transition regime with the $\pi/2$-limit regime from A to B. It can be observed that for the transition regime, the oscillation amplitude of the angle is larger, while at A the angle is closer to the $-\pi/4$ asymptotic limit. This larger-amplitude oscillation is accordingly more unstable.

3.4.2. *Wavy rotation regime and the multipeak subregimes*

As discussed in § 3.1, the wavy rotation regime indicates that the cylinder undergoes a large rotation in one direction followed by a slight reversal in the opposite direction periodically. The wavy rotation regime can be regarded as a mixture of the π-limit oscillation and autorotation regimes.

Similar to the last subsection, figure 10 represents the time history of typical quantities and marks six instants (A–F). The snapshots of the flow field are accordingly shown in figure 11.

As the square cylinder rotates to its minimum angle at A, a stagnation point is formed near corner 's', generating a clockwise moment. The cylinder approaches a symmetric diamond configuration, and two large recirculation regions are observed behind the two

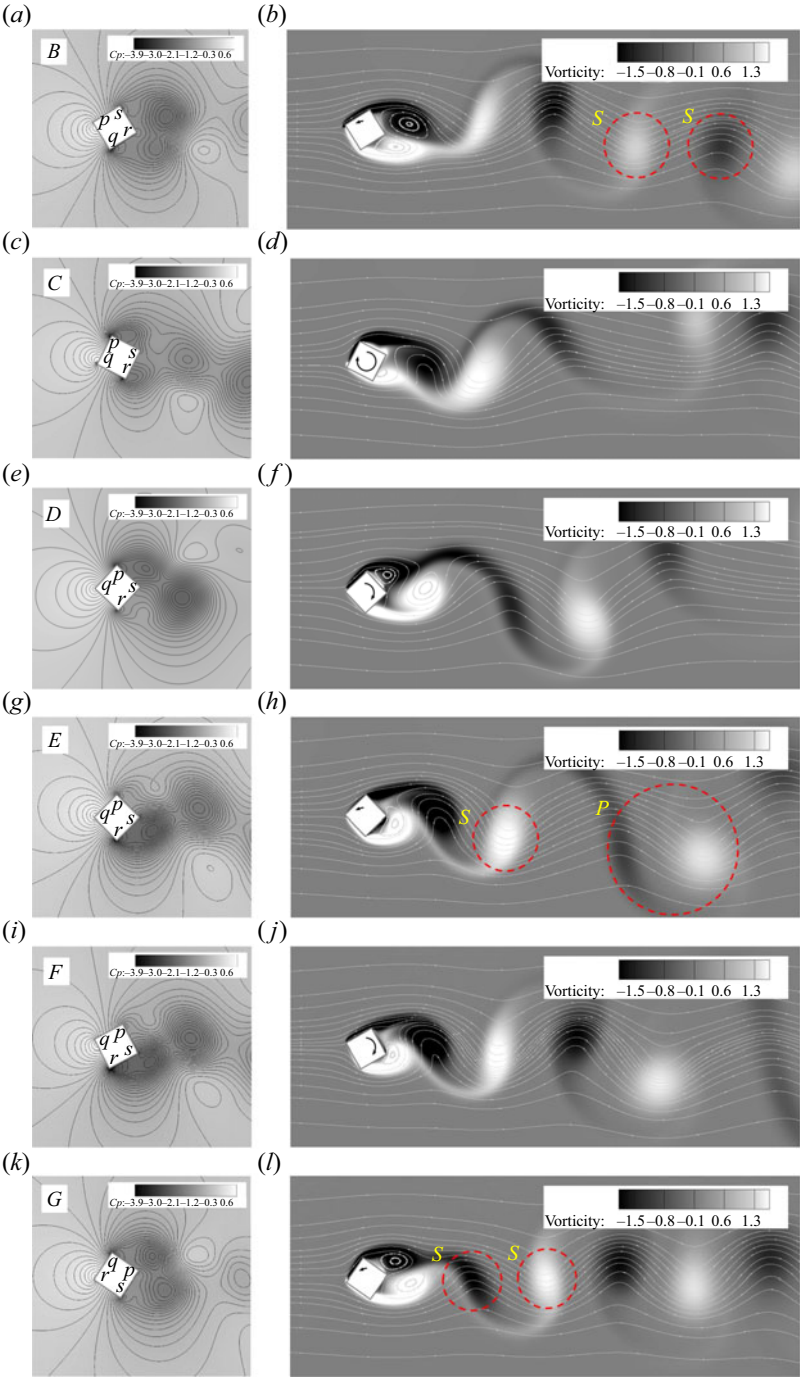

Figure 8. Pressure contours (*a*,*c*,*e*,*g*,*i*,*k*) and streamlines with spanwise vorticity contours (*b*,*d*,*f*,*h*,*j*,*l*) for the transition regime at six instants (*B* to *G*) marked in figure 7. The arrow inside the cylinder represents the angular velocity of cylinder.

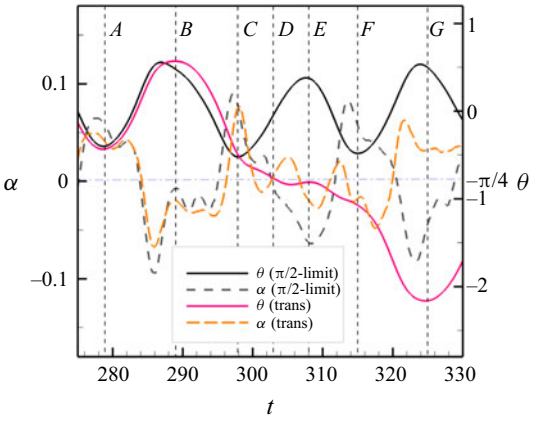

Figure 9. Comparison of angle θ and angular acceleration α, between the $\pi/2$-limit oscillation ($Re = 80$, $\rho = 2$, denoted as '$\pi/2$-limit') and transition regimes ($Re = 90$, $\rho = 4$, denoted as 'trans').

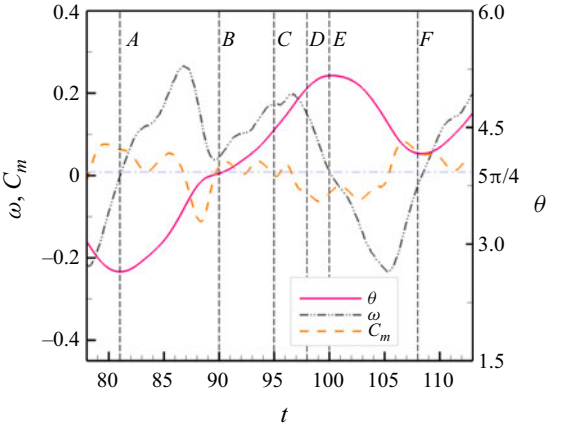

Figure 10. Time histories of the rotation angle θ, angular velocity ω and moment coefficient C_m, in a time interval for the transition regime ($Re = 140$, $\rho = 2.4$).

leeward faces. The pressure distributions on the two leeward faces are nearly symmetric, resulting in a net clockwise moment that drives the cylinder to rotate farther in the same direction.

At B, the cylinder and the recirculation zones near the two leeward sides have similar positions as at A. However, the stagnation pressure pocket is symmetrically located, and the net moment approaches zero. Due to inertia, the rotation angle θ exceeds the asymptotic value $5\pi/4$. It can be observed in figure 10 that C_m is a small positive value from B to C, resulting in the increasing angular velocity ω. At C, it can be observed in figure 11 that a stagnation point pressure pocket is located near the midpoint of this edge, while the recirculation zone is located directly behind the cylinder. The position of the stagnation pressure pocket and recirculation zone does not generate a significant rotational moment, leading to approximately zero C_m and consequently quasiconstant angular velocity from C to D. This situation changes at D since the stagnation pressure pocket moves closer to the corner 'q', leading to a clockwise moment and consequently decreasing angular velocity. The cylinder then stays at this position from D to E, corresponding to the fact

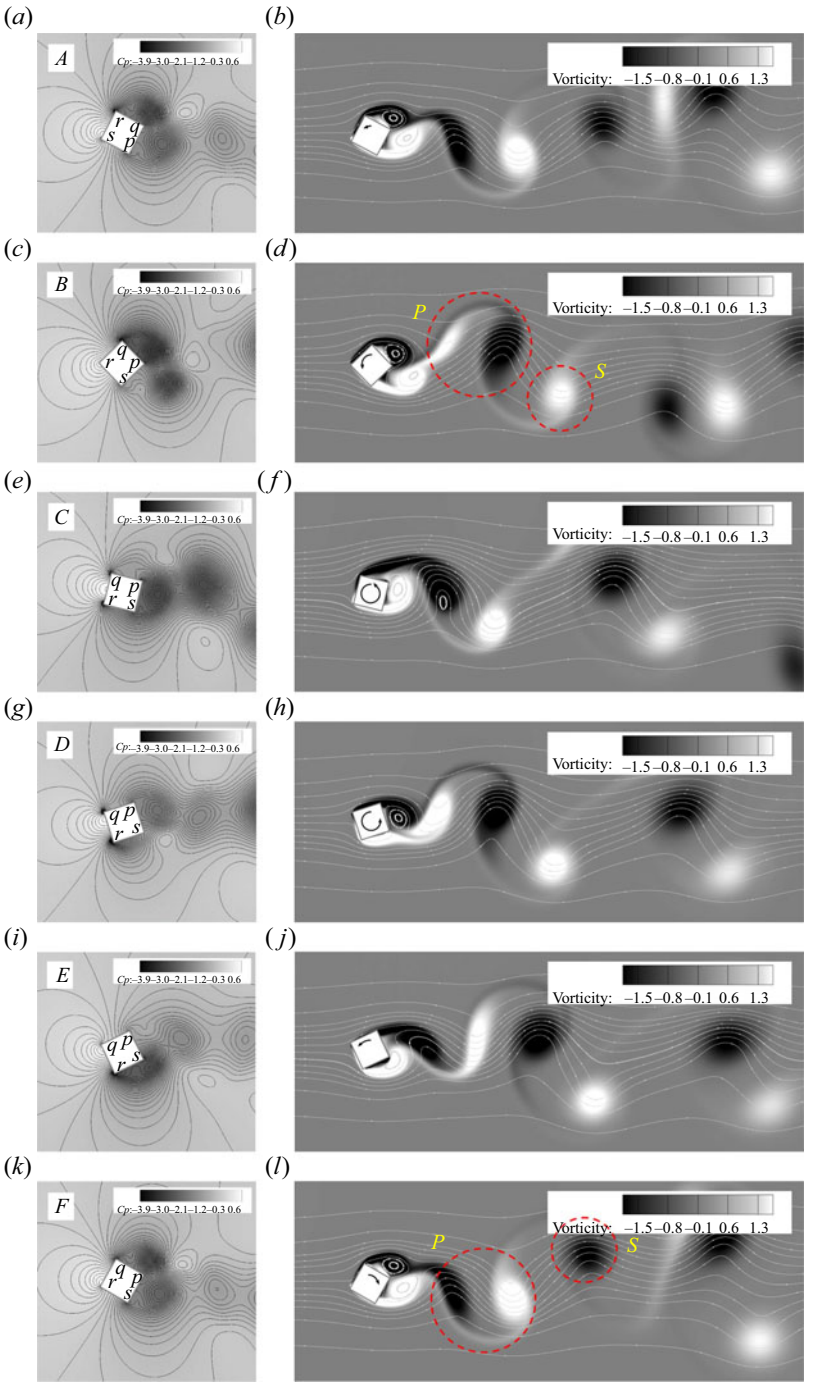

Figure 11. Pressure contours (*a*,*c*,*e*,*g*,*i*,*k*) and streamlines with spanwise vorticity contours (*b*,*d*,*f*,*h*,*j*,*l*) for wavy rotation regime at six instants (*A* to *F*) marked in figure 10. The arrow inside the cylinder represents the angular velocity of cylinder.

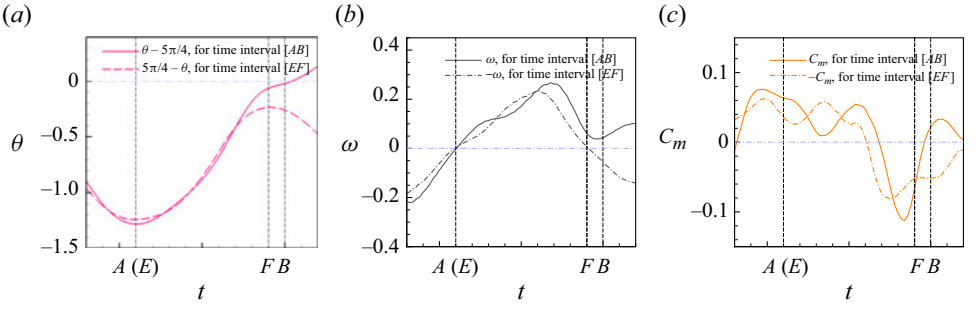

Figure 12. Comparison between the time intervals [*AB*] and [*EF*] in figure 10. (*a*) Rotation angle θ; (*b*) angular velocity ω; (*c*) moment coefficient C_m.

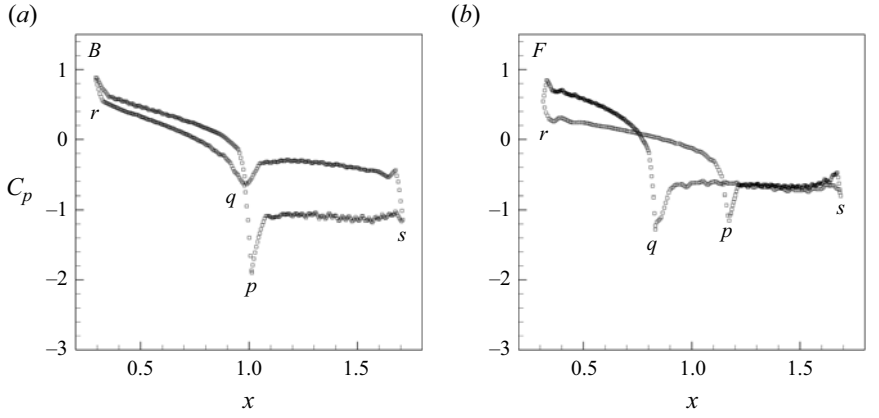

Figure 13. Distribution of pressure coefficient on the surface of cylinder, at (*a*) instant *B*, and (*b*) instant *F*, respectively. The instants are defined in figure 10.

that the stagnation pressure pocket remains similar, but vortex shedding happens on the leeward side. Finally, it can be observed in figure 10 that the kinetic quantities are very close between instants *A* and *F* (considering for a $\pi/2$ rotation for θ), indicating the start of another period. Note that the flow pattern in the downstream wake region is always the P+S mode, represented by the red circles in figure 11(*d*,*l*).

It is interesting to compare between the instants *B* and *F* in figure 10, which should be two similar peak instants for the $\pi/2$ regime (see figure 9 for example). We then put the evolution in time intervals [*AB*] and [*EF*] together for comparison, as shown in figure 12. As mentioned above, the time histories of θ, ω and C_m should all be symmetric between [*AB*] and [*EF*] if it is a $\pi/2$-limit regime, but differences exist in figure 12. For example, a qualitative difference exists for C_m between instants *B* and *F*: in figure 12(*c*), the value of C_m is nearly zero at *B*, but is non-zero at *F*. To dig a little more, in figure 13 we draw the distribution of pressure coefficient C_p, which is usually a dominant contribution for the moment (Ryu & Iaccarino 2017). From figure 13, it can be observed that all leeward faces (i.e. *qs* and *ps*) are affected by approximately constant pressure, leading to negligible contribution to the net moment. For the windward faces (i.e. *qr* and *pr*), at *B* the distributions are nearly symmetric, but at *F* it is obviously asymmetric and yields a net moment. In brief, we can summarize that the peaks of wavy rotation regime are principally affected by the symmetry properties of the windward faces.

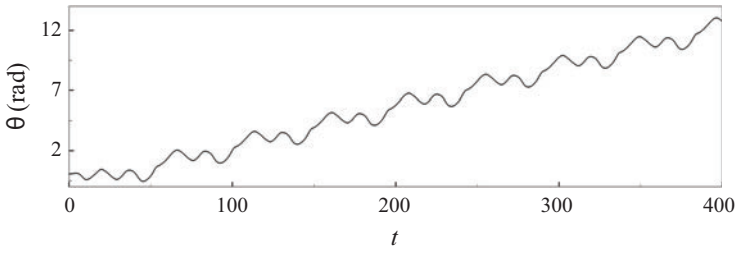

Figure 14. Time history of rotation angle of the 2-peak subregime in the wavy rotation regime ($Re = 140$, $\rho = 3.6$).

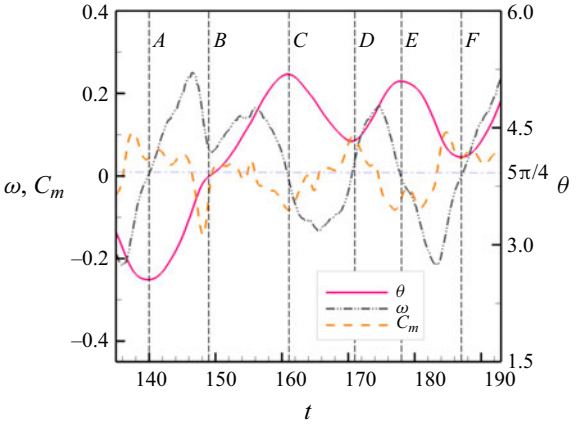

Figure 15. Time histories of rotation angle θ, angular velocity ω and moment coefficient C_m, in a time interval for the 2-peak subregime ($Re = 140$, $\rho = 3.6$) in the wavy rotation regime.

The above analysis describes the motion of the wavy rotation regime, in which we observe one peak and one valley of angular velocity in each period. However, this is not the only subregime of the wavy rotation regime. In fact, as indicated in figure 5, for $Re = 140$, $\rho = 3.6, 3.7$, we can observe another subregime of the wavy rotation regime, with two peaks and two valleys in each period (see figure 14). We will denote this as '2-peak subregime' as a specific response dynamics of the wavy rotation regime, while the case in figure 10 is denoted as '1-peak subregime' for clarity. The time histories of the dynamic quantities are shown in figure 15. The maximum angular velocity in this subregime is 0.250, which is lower than the value 0.269 in figure 10.

Comparison of angle θ and angular acceleration α between the 2-peak and 1-peak subregimes is shown in figure 16. The dynamics for these two subregimes is quite similar from A to C. The evolution of the 2-peak subregime is slightly slower than the 1-peak subregime, and θ reaches its peak value (at C) slightly later than the 1-peak subregime. This difference is accumulated, finally at E the 2-peak subregime does not have enough angular acceleration to switch to an autorotation state.

Further examinations can be performed by looking at the snapshots in figure 17. We can compare the instant C of figure 17 with the instant E of figure 11 since the positions of the cylinder are similar. A difference exists for the recirculation zone, which is quasisymmetric for instant C of the 2-peak subregime but asymmetric for instant E of the 1-peak subregime. The instant D of figure 17 is comparable to the instant F of figure 11

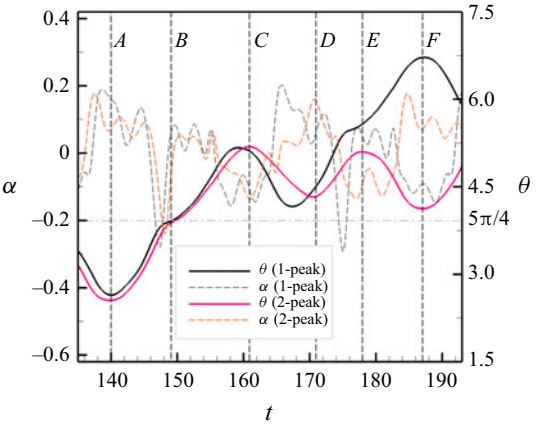

Figure 16. Comparison of angle θ and angular acceleration α, between the 2-peak subregime ($Re = 140$, $\rho = 3.6$) and the 1-peak subregime ($Re = 140$, $\rho = 2.4$) in the wavy rotation regime. Instants are defined as the same as figure 15.

as the angle evolutions are both in a valley; however, differences in the recirculation zone are more obvious. Finally, the instant E of figure 17 is comparable to the instant B of figure 11, while evident differences in the recirculation zone leads to different dynamics. To summarize, the difference between the 2-peak and 1-peak subregimes is caused by a gradual accumulation of angle difference from C to E (instants defined in figure 15).

3.4.3. *Multipeak subregimes in the π-limit oscillation regime*

As a complement to the observations in Ryu & Iaccarino (2017), we observed multipeak subregimes in the π-limit oscillation regime, as indicated in figure 5, namely the 2-peak and 3-peak subregimes. Typical time histories of these subregimes are shown in figures 18 and 19, respectively. For clarity, the dynamics of π-limit oscillation reported in Ryu & Iaccarino (2017) is specified as the 1-peak subregime. In this subsection the 2-peak subregime will be selected as an example to analyse, while for the 3-peak subregime the mechanism is similar.

Regarding the 2-peak subregime, the time histories of rotation angle θ, angular velocity ω and moment coefficient C_m in a period are shown in figure 20. This figure is comparable to the 1-peak subregime shown in figure 12 of Ryu & Iaccarino (2017). A difference between them is the maximal angular velocity, which is 0.253 for the 2-peak subregime and 0.318 for the 1-peak subregime. Qualitatively, this global lack of kinetic energy yields the generation of a second peak at instant D in figure 20. A detailed comparison can be found in figure 21.

The snapshots of the flow field at different instants (from A to F), defined in figure 21, are accordingly shown in figure 22. At A, the cylinder is close to a symmetric diamond shape, and there are two symmetrical large recirculation zones near the two leeward sides. The stagnation pressure pocket is located near the corner 'r' and the pressure distribution around the cylinder is nearly symmetrical. Therefore, the net moment at A is small but positive (anticlockwise) and drives the cylinder to rotate anticlockwise. At B, the angular velocity of the cylinder reaches a local minimum, but it is still positive. The moment approaches zero due to the symmetrical location of the stagnation pressure pocket. However, the moment after B becomes positive, which drives the cylinder to cross

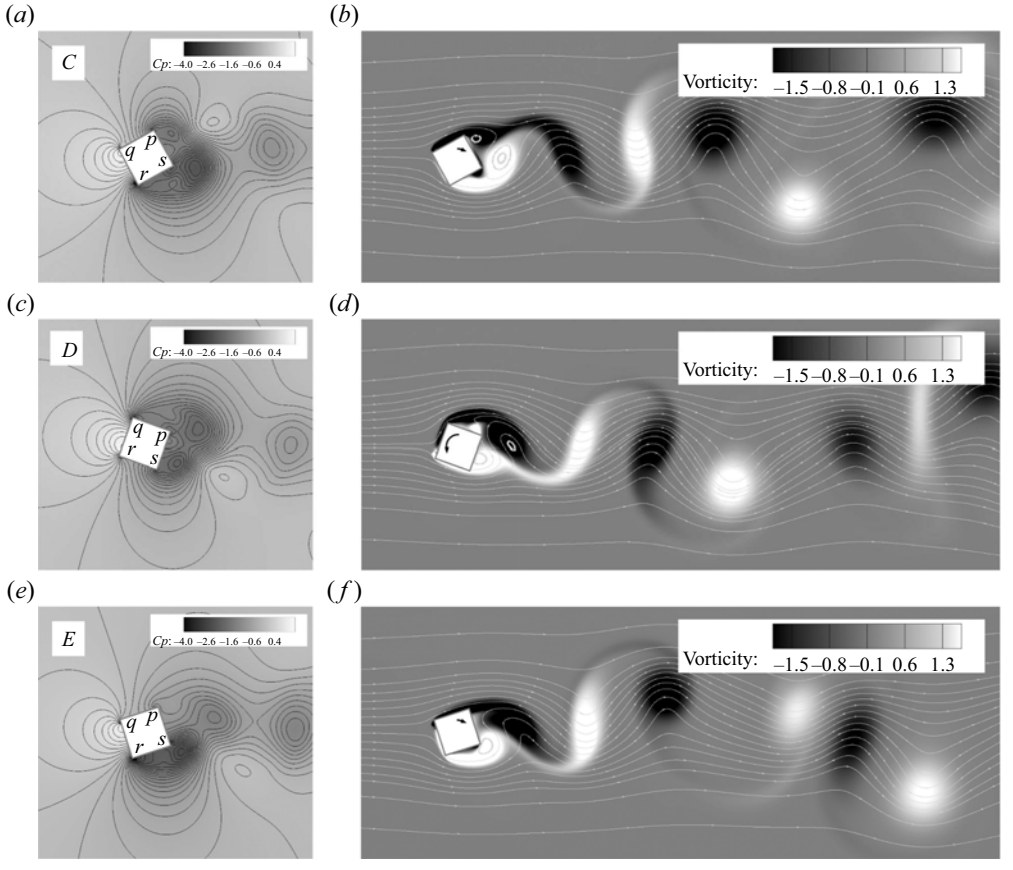

Figure 17. Pressure contours (*a*,*c*,*e*) and streamlines with spanwise vorticity contours (*b*,*d*,*f*) for the 2-peak subregime in the wavy rotation regime at three instants (*C*, *D*, *E*) marked in figure 15. The arrow inside the cylinder represents the angular velocity of cylinder.

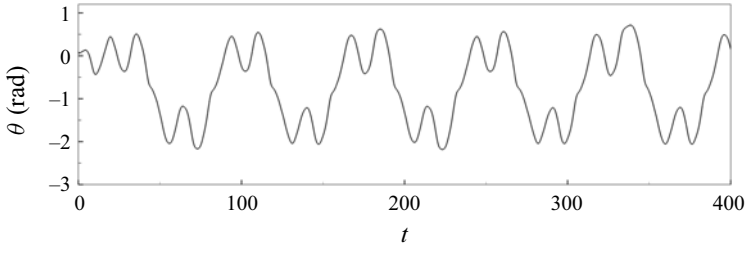

Figure 18. Time history of rotation angle of 2-peak subregime ($Re = 140$, $\rho = 3.1$) in the π-limit oscillation regime.

over the asymptotic limit $-\pi/4$. At *C*, the stagnation pressure pocket is near the corner '*p*', while the recirculation zone is near the leeward side, leading to a clockwise net moment. The moment reaches a local minimum and causes the cylinder to reverse its rotation to a clockwise direction. At *D*, the moment is anticlockwise, which differs from the case of the 1-peak subregime, and yields a second peak. Compared with the 1-peak subregime,

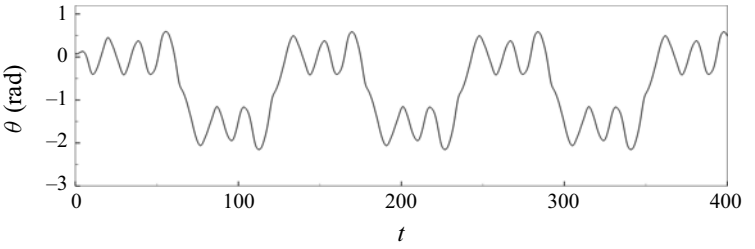

Figure 19. Time history of rotation angle of 3-peak subregime ($Re = 140$, $\rho = 3.9$) in the π-limit oscillation regime.

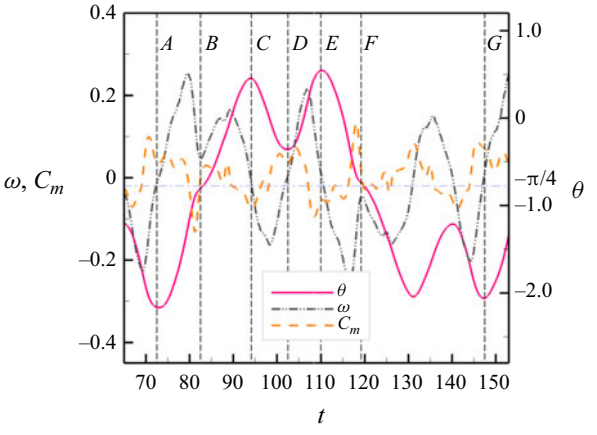

Figure 20. Time histories of rotation angle θ, angular velocity ω and moment coefficient C_m, in a time interval for the 2-peak subregime ($Re = 140$, $\rho = 3.1$) in the π-limit oscillation regime.

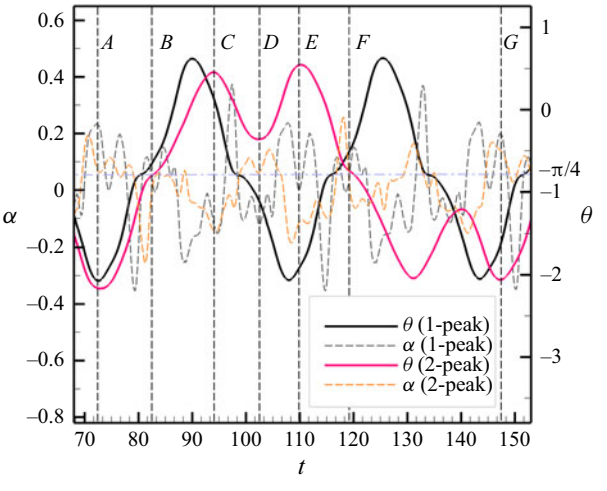

Figure 21. Comparison of angle θ and angular acceleration α, between the 2-peak subregime ($Re = 140$, $\rho = 3.1$) and the 1-peak subregime ($Re = 140$, $\rho = 1$) in the π-limit oscillation regime.

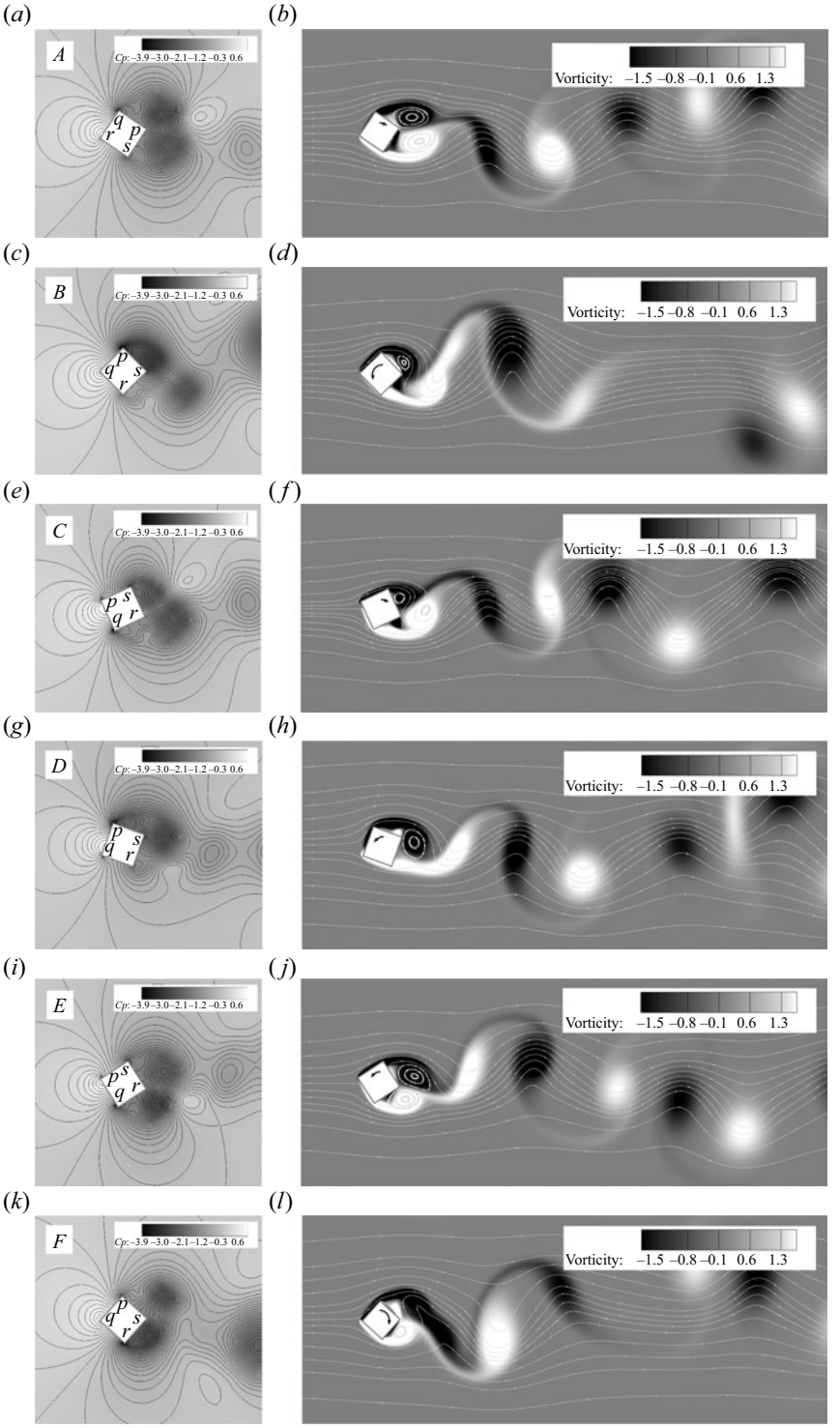

Figure 22. Pressure contours (*a*,*c*,*e*,*g*,*i*,*k*) and streamlines with spanwise vorticity contours (*b*,*d*,*f*,*h*,*j*,*l*) for the 2-peak subregime in the π-limit oscillation regime at six instants (*A*–*F*) indicated in figure 20. The arrow inside the cylinder represents the angular velocity of cylinder.

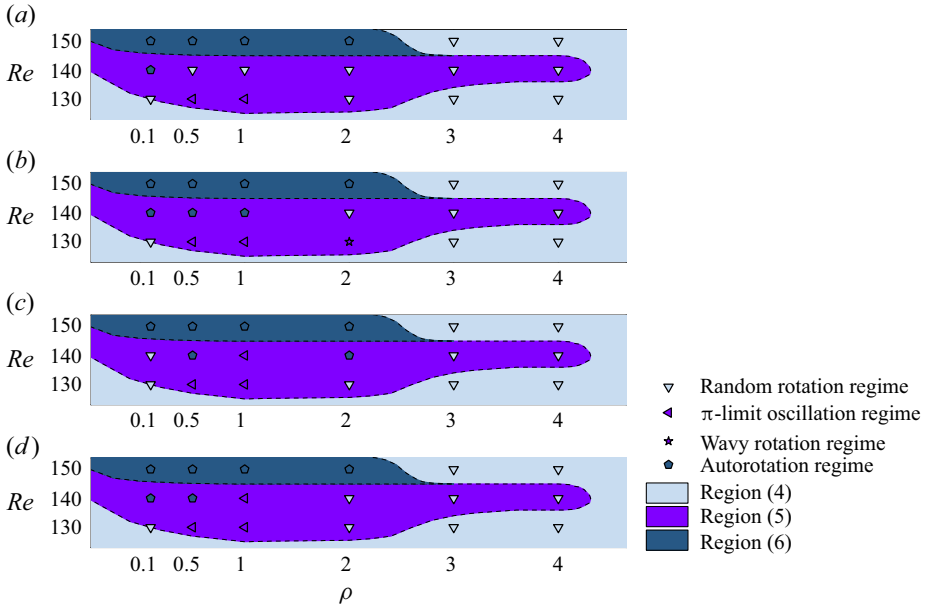

Figure 23. Regime distributions around region (5) defined in figure 4 with different initial angles: (*a*) $\theta_0 = 0.001$; (*b*) $\theta_0 = 0.01$; (*c*) $\theta_0 = 0.1$; (*d*) $\theta_0 = 0.5$. For comparison, region (6) and a part of region (4) are also shown.

the clockwise angular acceleration of the 2-peak subregime from *C* to *A* is weak. This prevents the cylinder from crossing over the $-\pi/4$ asymptotic limit.

3.5. *Multistable states*

The phenomenon of bistability has been observed in various problems of fluid–structure interactions, such as the forward and inverted flapping flags (Zhang *et al.* 2000; Zhu & Peskin 2002; Hao *et al.* 2012; Kim *et al.* 2012; Lee, Huang & Sung 2014; Tang, Liu & Lu 2015; Jia, Fang & Huang 2019). In numerical simulations, this phenomenon means that the regime of the structure response can be sensitive to initial conditions. In the present work, we use the similar strategy for the VIR of square cylinder. The initial angles are selected to be different values, i.e. $\theta_0 = 0.001$, 0.01, 0.1 and 0.5. Figure 23 shows the corresponding regimes around region (5) defined in figure 4. In fact, as illustrated in figure 5 with $\theta_0 = 0.1$, the region (5) can generate chaotic regimes and subregimes when the parameters are slightly changed. Here figure 23 further indicates that the responses are also sensitive to initial conditions. It is observed that for $\rho \leqslant 2$ in region (5), there exists bistable and multistable states. For example, for $Re = 140$ and $\rho = 1$, the four initial angles lead to three different regimes.

In order to further investigate the stability of these states, we select the case with $Re = 140$ and $\rho = 1$ as an example. As shown in figure 23, three regimes were observed at different initial angles. Here these regimes are examined with short-time perturbations, respectively. Specifically, additional clockwise or anticlockwise torque is externally added as a perturbation to observe the response of the cylinder. The amplitude of this perturbation is set to one-quarter of the maximum torque, while the time duration of the perturbation is set as 0.5.

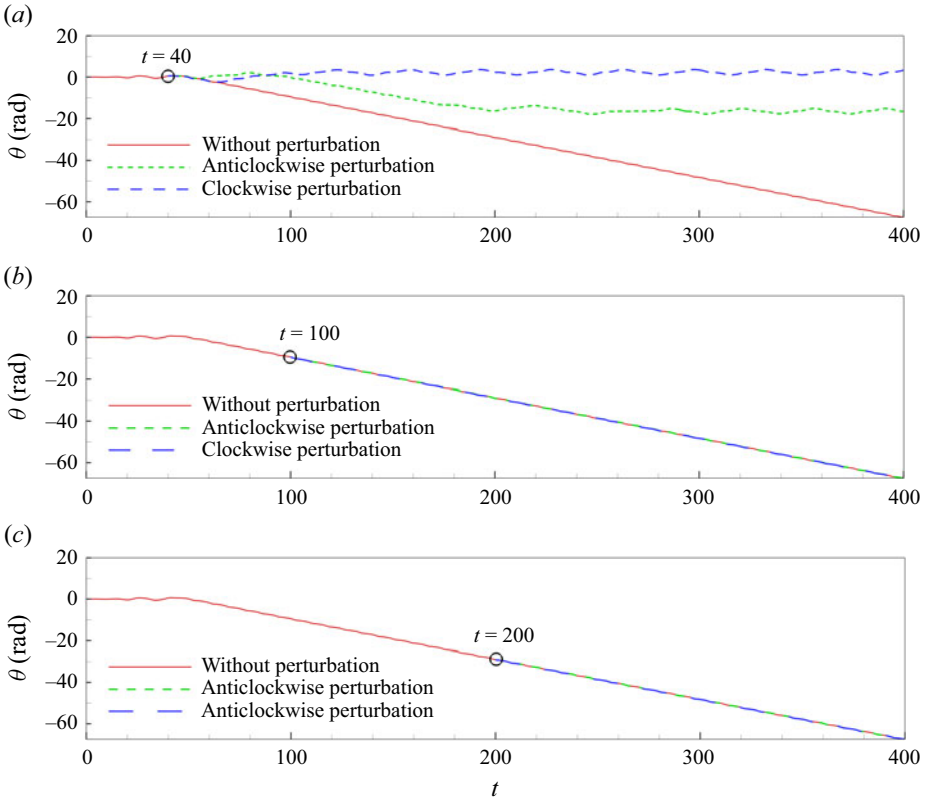

Figure 24. Time histories of the rotation angle of the autorotation regime ($Re = 140$, $\rho = 1$, $\theta_0 = 0.01$) with clockwise or anticlockwise perturbation at (*a*) $t = 40$, (*b*) $t = 100$ and (*c*) $t = 200$, respectively, comparing with the case without perturbation.

For the autorotation regime ($\theta_0 = 0.01$), perturbations are added at $t = 40$, $t = 100$ and $t = 200$, respectively, as shown in figure 24. From the response without perturbation, we can observe that the autorotation regime is established at approximately $t = 60$. Perturbations before this time (i.e. $t = 40$ as shown in figure 24*a*) lead to the π-limit oscillation regime, while perturbations after this time (i.e. $t = 100$ and 200 as shown in figure 24*b*,*c*) do not change the response of the autorotation regime. This indicates that the autorotation regime can be regarded as a phase-space region close to a stable attractive structure (for instance, a fixed point or a limit cycle). Early evolution ($t = 40$) corresponds to the stage that is not attracted to this structure yet, then small perturbations can turn to other attractive structures (π-limit oscillation regime here); by contrast, in later evolution ($t = 100$ and 200) the motion is attracted and cannot be simply perturbed.

For the π-limit oscillation regime ($\theta_0 = 0.1$), as shown in figure 25, the conclusion is similar. The anticlockwise perturbation before the establishment of the π-limit oscillation regime (i.e. $t = 100$ as shown in figure 25*a*) leads to a random rotation regime, while other perturbations do not change the response of the π-limit oscillation regime. Again, this indicates that the π-limit oscillation regime can also be regarded as a phase-space region close to a stable attractive structure.

For the random rotation regime ($\theta_0 = 0.001$), as shown in figure 26, results are more complicated. It is observed that the anticlockwise perturbation at $t = 100$ yields the

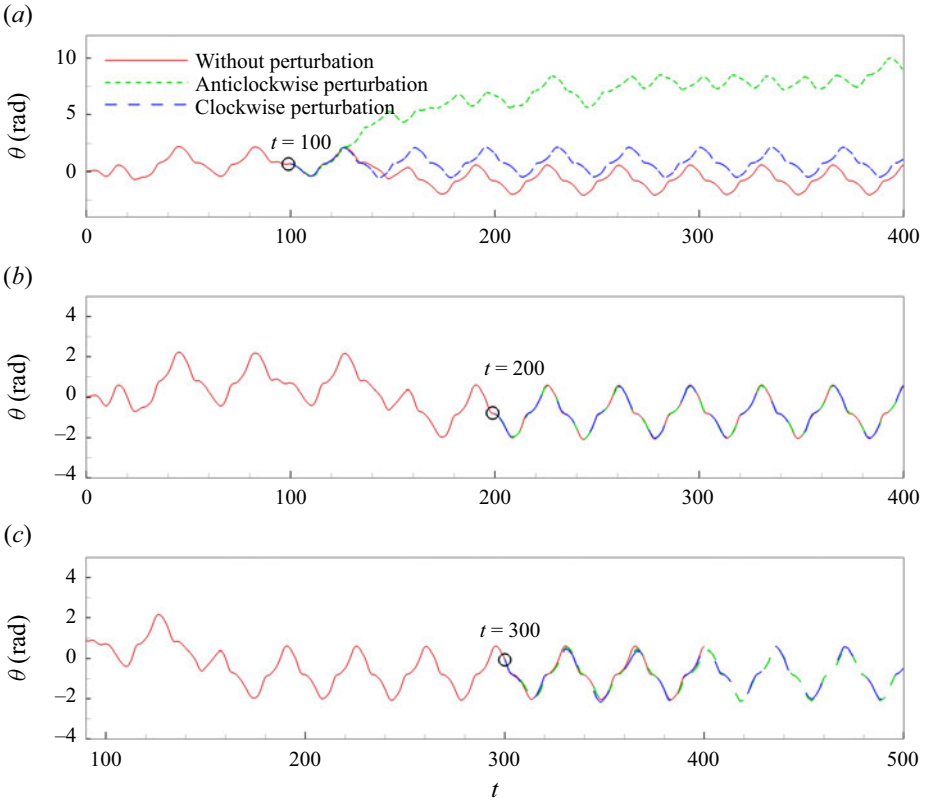

Figure 25. Time histories of the rotation angle of the π-limit oscillation regime ($Re = 140$, $\rho = 1$, $\theta_0 = 0.1$) with clockwise or anticlockwise perturbation at (*a*) $t = 100$, (*b*) $t = 200$ and (*c*) $t = 300$, respectively, comparing with the case without perturbation.

autorotation regime, the clockwise perturbation at $t = 200$ yields a random rotation regime, while all other perturbations lead to the π-limit oscillation regime. A way to explain this fact is to consider the random rotation regime as a motion in phase space which is not attracted by any stable structure, and a perturbation can turn it to any stable structure. A similar sketch of this mechanism can refer to figure 4 of Kerswell (2018). In this sense, although the random rotation regime is regarded as a stable state since the regime can remain for enough of a long time, it differs from the concept of stable equilibrium defined in autonomous systems.

To summarize, we argue that the multistable states in region (5) are results of the existence of multiple stable attractive structures in phase space. This explanation indicates a different mechanism by comparing with the bistable states of flexible flags which were explained as a hysteresis process between two modes (Kim *et al.* 2012; Lee *et al.* 2014). An analogical phenomenon might be the bistable states of freely falling heavy plates (Lau, Huang & Xu 2018), resulting from the competition of unsteady flow and object inertia.

4. Conclusion

In this paper, the VIR of a square cylinder under the influence of Reynolds number and density ratio is investigated by using numerical simulations. Regimes are summarized and classified in figure 4. Cases with a fixed density ratio show good agreement with Ryu &

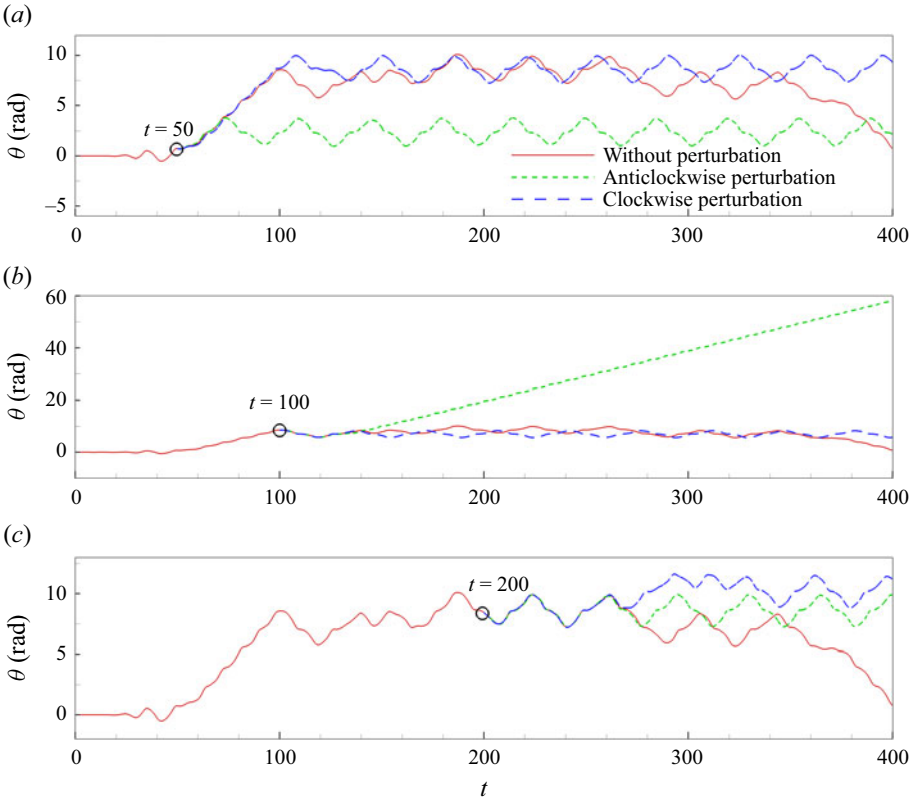

Figure 26. Time histories of the rotation angle of the random rotation regime ($Re = 140$, $\rho = 1$, $\theta_0 = 0.001$) with clockwise or anticlockwise perturbation at (*a*) $t = 50$, (*b*) $t = 100$ and (*c*) $t = 200$, respectively, comparing with the case without perturbation.

Iaccarino (2017), while changing the density ratio leads to more complicated distribution of regimes and subregimes. The main conclusions are listed as follows.

(*a*) A phenomenon related to the influence of density ratio is the tooth-like shape of the $\pi/2$-limit oscillation regime, observed in the regime map. This phenomenon can be explained as a result of the imbalance relation between the main frequencies of rotation response and the vortex shedding frequency.

(*b*) A transition regime is observed, behaving as a mixture of the $\pi/2$-limit oscillation and random rotation regimes. Specifically, the regime randomly switches between different quasi-$\pi/2$-limit oscillation regimes with different quasiequilibrium angles.

(*c*) A wavy rotation regime is observed, indicating that in a period, the cylinder rotates for a large angle in a certain direction and then reverses its rotation for a small angle. Moment-generating mechanisms suggest that the peaks of the wavy rotation regime are principally affected by the symmetry properties of the windward faces. In addition, the wavy rotation regime can be classified into subregimes, according to the number of peaks in a period.

(*d*) In the π-limit oscillation regime, new subregimes are observed, which are defined according to the number of peaks in a period. The multipeak subregimes correspond to the process of accumulating kinetic energies.

(*e*) The region (5) defined in figure 4 contains multiple regimes, which are generated without regularity with the same initial condition (see figure 5). Furthermore, changing initial conditions can also lead to multistable states for the same Reynolds number and density ratio. Comparing with existing observations of bistable states in other problems of fluid–structure interactions, with the same Reynolds number and density ratio, changing initial conditions can yield up to different regimes. These multistable states are probably results of the existence of multiple stable attractive structures in phase space.

Funding. We thank Z. Li for helpful discussions. This work was supported by the National Natural Science Foundation of China (project approval nos. 12372214, 52105083, 12272206, 92252204 and 12388101) and the Science Center for Gas Turbine Project (grant no. P2022-C-III-001-001).

Declaration of interests. The authors report no conflict of interest.

Author ORCIDs.
Rui-Yong Mou https://orcid.org/0000-0001-6408-3202;
Wei-Xi Huang https://orcid.org/0000-0003-4149-3369;
Le Fang https://orcid.org/0000-0001-5756-7102.

References

Amandolèse, X. & Hémon, P. 2010 Vortex-induced vibration of a square cylinder in wind tunnel. *C. R. Méc.* **338** (1), 12–17.

Arnal, M.P., Goering, D.J. & Humphrey, J.A.C. 1991 Vortex shedding from a bluff body adjacent to a plane sliding wall. *Trans. ASME J. Fluids Engng* **113**, 384–398.

Assi, G.R.S., Bearman, P.W. & Meneghini, J.R. 2010 On the wake-induced vibration of tandem circular cylinders: the vortex interaction excitation mechanism. *J. Fluid Mech.* **661**, 365–401.

Bao, Y., Wu, Q. & Zhou, D. 2012 Numerical investigation of flow around an inline square cylinder array with different spacing ratios. *Comput. Fluids* **55**, 118–131.

Bearman, P.W. 2011 Circular cylinder wakes and vortex-induced vibrations. *J. Fluids Struct.* **27** (5–6), 648–658.

Cheng, L., Zhou, Y. & Zhang, M.M. 2003 Perturbed interaction between vortex shedding and induced vibration. *J. Fluids Struct.* **17** (7), 887–901.

Cheng, M., Whyte, D.S. & Lou, J. 2007 Numerical simulation of flow around a square cylinder in uniform-shear flow. *J. Fluids Struct.* **23** (2), 207–226.

Griffin, O.M. 1985 Vortex shedding from bluff bodies in a shear flow: a review. *Trans. ASME J. Fluids Engng* **107**, 298–306.

Han, P. & de Langre, E. 2022 There is no critical mass ratio for galloping of a square cylinder under flow. *J. Fluid Mech.* **931**, A27.

Hao, H.-T., Qin, F.-H., Huang, W.-X. & Sun, D.-J. 2012 Multiple modes of filament flapping in a uniform flow. *Chin. Phys. Lett.* **29** (9), 094702.

Huang, W.X., Shin, S.J. & Sung, H.J. 2007 Simulation of flexible filaments in a uniform flow by the immersed boundary method. *J. Comput. Phys.* **226** (2), 2206–2228.

Jia, K., Fang, L. & Huang, W.X. 2019 Coupled states of dual side-by-side inverted flags in a uniform flow. *J. Fluids Struct.* **91**, 102768.

Jiang, X., Andreopoulos, Y., Lee, T. & Wang, Z. 2016 Numerical investigations on the vortex-induced vibration of moving square cylinder by using incompressible lattice Boltzmann method. *Comput. Fluids* **124**, 270–277.

Juarez, H., Scott, R., Metcalfe, R. & Bagheri, B. 2000 Direct simulation of freely rotating cylinders in viscous flows by high-order finite element methods. *Comput. Fluids* **29** (5), 547–582.

Kerswell, R.R. 2018 Nonlinear nonmodal stability theory. *Annu. Rev. Fluid Mech.* **50**, 319–345.

Kim, B., Huang, W.-X., Shin, S.J. & Sung, H.J. 2012 Flexible ring flapping in a uniform flow. *J. Fluid Mech.* **707**, 129–149.

Lau, E.M., Huang, W.-X. & Xu, C.-X. 2018 Progression of heavy plates from stable falling to tumbling flight. *J. Fluid Mech.* **850**, 1009–1031.

LEE, J.H., HUANG, W.-X. & SUNG, H.J. 2014 Flapping dynamics of a flexible flag in a uniform flow. *Fluid Dyn. Res.* **46**, 055517.

LUGT, H.J. 1980 Autorotation of an elliptic cylinder about an axis perpendicular to the flow. *J. Fluid Mech.* **99** (4), 817–840.

LUGT, H.J. 1983 Autorotation. *Annu. Rev. Fluid Mech.* **15**, 123–147.

LUO, C.S., MOU, R.Y., HUANG, X.R., HUANG, W.X. & FANG, L. 2023 A free-streamline boundary-layer model for small-amplitude oscillation regime of square cylinder under vortex-induced rotation. *Phys. Fluids* **35**, 093602.

MINEWITSCH, S., FRANKE, R. & RODI, W. 1994 Numerical investigation of laminar vortex-shedding flow past a square cylinder oscillating in line with the mean flow. *J. Fluids Struct.* **8** (8), 787–802.

MITTAL, S., KUMAR, V. & RAGHUVANSHI, A. 1997 Unsteady incompressible flows past two cylinders in tandem and staggered arrangements. *Intl J. Numer. Meth. Fluids* **25** (11), 1315–1344.

PAN, Z., CHEN, Z. & WU, H. 2019 Self-excited rotation and flow dynamics across a freely rotatable square cylinder confined between two parallel walls. *Phys. Fluids* **31** (8), 087109.

PARK, Y.G., MIN, G., HA, M.Y. & YOON, H.S. 2015 Response characteristics of vortex around the fixed and freely rotating rectangular cylinder with different width to height ratios. *Prog. Comput. Fluid Dyn.* **15** (1), 1–9.

QIU, T., XU, Q., DU, X., ZHAO, Y. & LIN, W. 2022 VIV of twin square cylinders in various configurations at a low Reynolds number. *Ocean Engng* **260**, 112067.

ROBERTSON, I., LI, L., SHERWIN, S.J. & BEARMAN, P.W. 2003 A numerical study of rotational and transverse galloping rectangular bodies. *J. Fluids Struct.* **17** (5), 681–699.

RYU, S. 2018 Quadrant analysis on vortex-induced autorotation of a rigid square cylinder. *J. Mech. Sci. Technol.* **32** (6), 2629–2635.

RYU, S. & IACCARINO, G. 2017 Vortex-induced rotations of a rigid square cylinder at low Reynolds numbers. *J. Fluid Mech.* **813**, 482–507.

SARPKAYA, T. 2004 A critical review of the intrinsic nature of vortex-induced vibrations. *J. Fluids Struct.* **19** (4), 389–447.

SEN, S., MITTAL, S. & BISWAS, G. 2011 Flow past a square cylinder at low Reynolds numbers. *Intl J. Numer. Meth. Fluids* **67** (9), 1160–1174.

SHAO, J., SHU, C., LIU, N. & ZHAO, X. 2019 Numerical investigation of vortex induced rotation of two square cylinders in tandem arrangement. *Ocean Engng* **171**, 485–495.

SOHANKAR, A., NORBERGB, C. & DAVIDSON, L. 1997 Numerical simulation of unsteady low-Reynolds number flow around rectangular cylinders at incidence. *J. Wind Engng Ind. Aerodyn.* **69–71**, 189–201.

TANG, C., LIU, N.S. & LU, X.Y. 2015 Dynamics of an inverted flexible plate in a uniform flow. *Phys. Fluids* **27** (7), 073601.

TAYLOR, I. & VEZZA, M. 1999 Calculation of the flow field around a square section cylinder undergoing forced transverse oscillations using a discrete vortex method. *J. Wind Engng Ind. Aerodyn.* **82** (1–3), 271–291.

WANG, H., YAN, Y., CHEN, C., JI, C. & ZHAI, Q. 2019 Numerical investigation on vortex-induced rotations of a triangular cylinder using an immersed boundary method. *China Ocean Engng* **33** (6), 723–733.

WANG, S., ZHU, L., ZHANG, X. & HE, G. 2011 Flow past two freely rotatable triangular cylinders in tandem arrangement. *Trans. ASME J. Fluids Engng* **133** (8), 081202.

WILLIAMSON, C.H.K. 1989 Oblique and parallel modes of vortex shedding in the wake of a circular cylinder at low Reynolds numbers. *J. Fluid Mech.* **206**, 579–627.

WILLIAMSON, C.H.K. & GOVARDHAN, R. 2004 Vortex-induced vibrations. *Annu. Rev. Fluid Mech.* **36** (1), 413–455.

WILLIAMSON, C.H.K. & ROSHKO, A. 1988 Vortex formation in the wake of an oscillating cylinder. *J. Fluids Struct.* **2** (4), 355–381.

XIA, Y., LIN, J., KU, X. & CHAN, T. 2018 Shear-induced autorotation of freely rotatable cylinder in a channel flow at moderate Reynolds number. *Phys. Fluids* **30** (4), 043303.

YOON, D.H., YANG, K.S. & CHOI, C.B. 2010 Flow past a square cylinder with an angle of incidence. *Phys. Fluids* **22** (4), 043603.

ZAKI, T.G., SEN, M. & GAD-EL-HAK, M. 1994 Numerical and experimental investigation of flow past a freely rotatable square cylinder. *J. Fluids Struct.* **8** (7), 555–582.

ZHANG, B., MAO, Z., SONG, B., DING, W. & TIAN, W. 2018 Numerical investigation on effect of damping-ratio and mass-ratio on energy harnessing of a square cylinder in FIM. *Energy* **144**, 218–231.

ZHANG, J., CHILDRESS, S., LIBCHABER, A. & SHELLEY, M. 2000 Flexible filaments in a flowing soap film as a model for one-dimensional flags in a two-dimensional wind. *Nature* **835**, 835–839.

ZHU, L. & PESKIN, C.S. 2002 Simulation of a flapping flexible filament in a flowing soap film by the immersed boundary method. *J. Comput. Phys.* **179** (2), 452–468.